

19. Schön, J. H. *et al.* Gate-induced superconductivity in solution-processed, organic polymer films. *Nature* **410**, 189–192 (2001).
20. Blanc, H.-B. *et al.* Single-crystal X-ray diffraction study of the room temperature structure and orientational disorder of C_{70} . *Europhys. Lett.* **27**, 359–364 (1994).
21. Blanc, E., Bürgi, H.-B., Restori, R., Schwarzenbach, D. & Ochsnein, Ph. X-ray diffraction study of the stacking faults in hexagonal C_{70} single crystals. *Europhys. Lett.* **33**, 205–210 (1996)
22. Bürgi, H. B. *et al.* The structure of C_{60} : orientational disorder in the low-temperature modification of C_{60} . *Angew. Chem. Int. Edn Engl.* **31**, 640–643 (1992).
23. Wang, Z. H. *et al.* Electronic properties of K_xC_{70} thin films. *Phys. Rev. B* **48**, 10657–10660 (1994).
24. Ohno, K., Jing-Zhi, Y., Maruyama, Y., Kawazoe, Y. & Takahashi, T. Electronic structures of C_{70} crystalline phases. *Chem. Phys. Lett.* **255**, 367–372 (1996).
25. Golden, M. S. *et al.* The electronic structure of fullerenes and fullerene compounds from high-energy spectroscopy. *J. Phys. Condens. Matter* **7**, 8219–8247 (1995).
26. Kobayashi, M. *et al.* Structure sequence and possible superconductivity in potassium-doped fullerene $C_{70}K_x$. *Phys. Rev. B* **48**, 16877–16880 (1993).
27. Schluter, M., Lannoo, M., Needles, M. & Baraff, G. A. Electron-phonon coupling and superconductivity in alkali-intercalated C_{60} solid. *Phys. Rev. Lett.* **68**, 526–529 (1992).

Acknowledgements

Access to beamline I711 at the MAX-II synchrotron storage ring in Lund is acknowledged.

Correspondence and requests for materials should be addressed to B.B. (e-mail: batlogg@solid.phys.ethz.ch).

Magma storage beneath Axial volcano on the Juan de Fuca mid-ocean ridge

M. West*†, W. Menke*†, M. Tolstoy*, S. Webb*† & R. Sohn‡

* Lamont-Doherty Earth Observatory of Columbia University, Palisades, New York 10964, USA

† Department of Earth and Environmental Science, Columbia University, Palisades, New York 10964, USA

‡ Woods Hole Oceanographic Institution, Woods Hole, Massachusetts 02543, USA

Axial volcano, which is located near the intersection of the Juan de Fuca ridge and the Cobb–Eickelberg seamount chain beneath the northeast Pacific Ocean, is a locus of volcanic activity thought to be associated with the Cobb hotspot¹. The volcano rises 700 metres above the ridge, has substantial rift zones extending about 50 kilometres to the north and south, and has erupted as recently as 1998 (ref. 2). Here we present seismological data that constrain the three-dimensional velocity structure beneath the volcano. We image a large low-velocity zone in the crust, consisting of a shallow magma chamber and a more diffuse reservoir in the lower crust, and estimate the total magma volume in the system to be between 5 and 21 km³. This volume is two orders of magnitude larger than the amount of melt emplaced during the most recent eruption^{3,4} (0.1–0.2 km³). We therefore infer that such volcanic events remove only a small portion of the reservoir that they tap, which must accordingly be long-lived compared to the eruption cycle. On the basis of magma flux estimates, we estimate the crustal residence time of melt in the volcanic system to be a few hundred to a few thousand years.

Axial volcano is formed by excess magmatism associated with mantle melting at the Cobb hotspot and the Juan de Fuca ridge⁵. Shoaling bathymetry, inferred crustal thickening⁶, frequent seismic swarms^{7,8} and deformation events^{3,4} are consistent with a robust magma supply system. Lateral dyke injection, observed during a 1998 eruption⁹, originated from a source under the caldera and carried magma up to 50 km along the volcano’s rift zones, which are substantial constructional features. Such events suggest that magma supply is strongly focused beneath the volcano. The existence of the 3 × 8 km caldera, its 3 m subsidence during the 1998 eruption¹⁰, and evidence for low-density rock beneath the summit¹¹, suggest a large

magma body a few kilometres beneath the volcano. What has not been understood is how much melt exists, how long it spends in the crust, and how eruptions along the rifts and adjacent ridge segments are related to the magma reservoir. These questions have remained unanswered, not just at Axial volcano, but at basaltic shield volcanoes worldwide.

The compressional-velocity image of the volcano presented here is based on data collected during a 1999 active-source seismic experiment (Fig. 1). 5,025 shots from the airgun array (20 guns totalling 142 litres) of the RV *Maurice Ewing* were recorded on six ocean-bottom seismometers¹² deployed on the volcano’s flanks. Water wave travel times and global positioning system (GPS)-determined shot locations were used to precisely locate the seismometers on the sea floor (error < 20 m) and to determine clock drifts (error < 0.02 s). Travel times from 16,400 Pg phases, which turn within the crust, are used in this study.

To characterize the regional structure, a bathymetry-draped one-dimensional (1D) velocity model was assembled from previous studies^{13,14} on the Juan de Fuca ridge. Predicted travel-time errors through this model were inverted to determine the best-fit 1D velocity structure (see Methods). Seismic ray-paths crossing the caldera were excluded from the inversion, so the resulting model represents average crustal structure away from the volcano. In the final 1D model (not shown), velocity contours 4–6 km s⁻¹ are up to 1 km deeper than on other parts of the Juan de Fuca^{13,14} ridge. The additional 0.5–1.0 km of volcanic extrusives implied by these depressed velocities is not surprising, considering the shallow bathymetry and crustal thickening⁶.

Seismic travel-time prediction was accomplished through a fast ray shooting method performed on a three-dimensional tetrahedral velocity grid. Predicted travel times through the 1D model deviate from real data with an r.m.s. error of 0.181 s. Much of this misfit is contributed by a small number of caldera-crossing rays which are systematically delayed by up to 0.5 s (Fig. 2). A three-dimensional

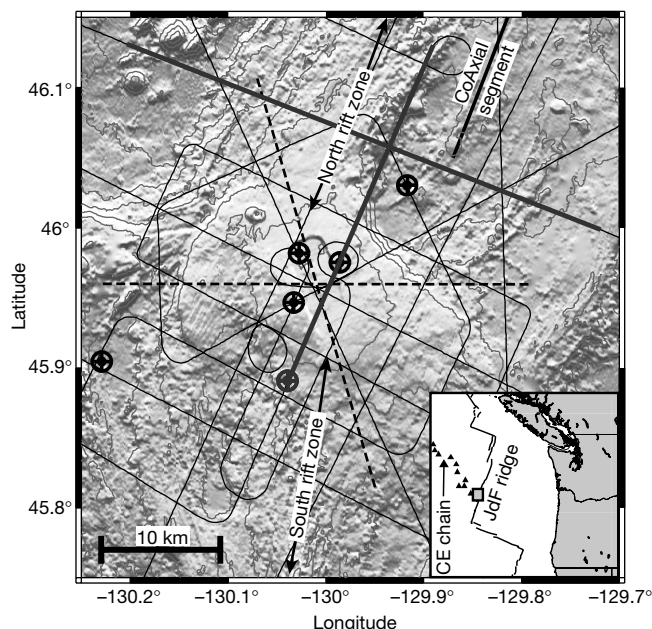


Figure 1 Bathymetry of Axial volcano. Summit caldera, in centre of figure, is at ~1,460 m depth, surrounding sea floor is at ~2,800 m depth, contour interval is 200 m. Thin black lines mark airgun shot lines, crossed circles with central dot show ocean-bottom seismometers used in analysis. Two dashed lines mark cross-sections in Fig. 4. The two crossing thick black lines, one of which ends in a seismometer, display source–receiver geometry for Fig. 2. Scale bar, 10 km. Inset, location of experiment on the Juan de Fuca (JdF) ridge, and the seamounts in the Cobb–Eickelberg (CE) chain.

(3D) tomographic inversion of the travel-time data, starting with the 1D model, was performed to determine a more realistic crustal structure. The final structure derived from the full set of Pg travel times reduced the travel-time misfit to 0.089 s. Chequerboard resolution tests demonstrate that this method and ray geometry are sufficient to resolve the features discussed here (Fig. 3).

A prominent low-velocity zone is centred directly beneath the caldera. It is oval in map view (8 × 12 km elongated northwest–southeast), and has a compressional velocity that is more than 2 km s⁻¹ (34%) slower than its surroundings (Fig. 4). The strongest anomaly (>15%) is confined to depths of 2.25–3.5 km below the sea floor. Perturbations of 0.5–1.0 km s⁻¹ extend to 5–6 km depth, beyond which the structure is not constrained. The low-velocity feature does not extend under the imaged portion of the rift zones or towards the nearby Vance or CoAxial segments of the Juan de Fuca ridge. The low-velocity anomaly is comparable in depth, twice the width and much larger in amplitude than a similar feature under the Kilauea caldera in Hawaii¹⁵.

Sub-solidus temperature differences can explain some of the low-velocity anomaly under the caldera. We determine the largest possible effect that temperature could have, using an approach similar to that of refs 16 and 17. We assume that the crust beneath the caldera is heated to the 1,150 °C basalt solidus¹⁸ (the highest temperature without the presence of melt); we also assume that the surrounding area has the cooler thermal structure given in Fig. 7f of

Table 1 Parameters used in melt estimates

Parameter	Value	Description
$\partial \ln v_p / \partial T$ at $T < 800$ °C*	$-8.1 \times 10^{-5} \% \text{ K}^{-1}$	Anharmonic effect only ²⁰
$\partial \ln v_p / \partial T$ at $T > 800$ °C	$-16 \times 10^{-5} \% \text{ K}^{-1}$	Anharmonic+anelastic effects ²¹ at 1,150 °C solidus ¹⁸ , $Q = 100$ (ref. 22)
$\partial \ln v_p / \partial F$ (max. melt)	-1.0%	Unrelaxed tubule-shaped inclusions ²⁷
$\partial \ln v_p / \partial F$ (min. melt)	-4.8%	Relaxed random cusped films above $F = 1\%$ (ref. 27)

v_p , P-wave velocity; T , temperature; F , melt fraction.
* Anelastic effects are considered for $T > 800$ °C. Above this temperature Q_{gabbro} drops below 500 (ref. 23), where $1/Q$ is the seismic attenuation. Used in Karato²² equation (6).

ref. 19, for 10 km off the axis of an intermediate-rate spreading ridge. The temperature difference as a function of depth is converted to a velocity perturbation using derivatives of compressional-wave velocity with respect to temperature²⁰ (Table 1). The effect of anelasticity is incorporated for temperatures > 800 °C (refs 21, 22). Up to 0.7 km s⁻¹ of the low-velocity anomaly can be explained by thermal effects below the solidus. Errors associated with the thermal assumptions are minimal. Shifting the solidus or the temperature profile by 100 °C changes the velocity effect by < 0.1 km s⁻¹. Microearthquakes in the caldera region, which constrain the depth of the brittle–plastic transition in crustal rheology^{23,24}, do not extend deeper than 2 km, indicating that the magma chamber is overlain by a hot, conductive lid approximately

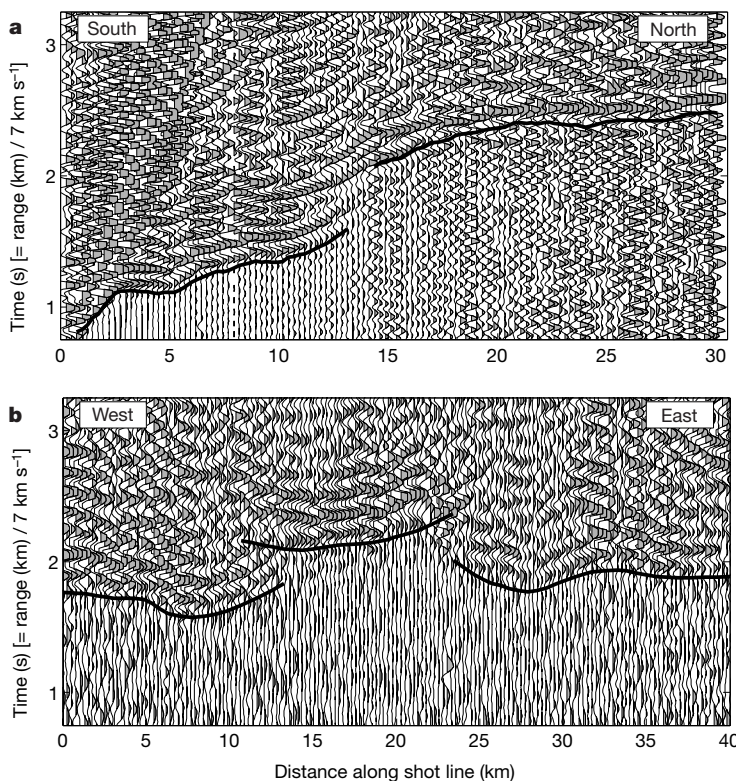


Figure 2 Example record sections showing the low-velocity zone. Shot–receiver geometries are marked on Fig. 1. A bandpass filter and a static topography correction have been applied to each record for display purposes. **a**, Straight line receiver gather. The first-arrival Pg phase is abruptly terminated at a range of 13 km from the receiver. At greater distances, the first significant arrival is delayed by 0.5 s. This phase corresponds to energy refracting through the deeper parts of the low-velocity zone. A similar shadow zone is observed on numerous shot–receiver geometries which cross the caldera. Rays with ranges > 13 km pass unaffected above the low-velocity zone. This record demonstrates that the low-velocity zone begins at depth beneath the caldera, and does not extend into the shallowest crust. **b**, Fan shot receiver gather. Shot–receiver ranges

are 20–29 km (too close for P_mP Moho reflection in the region). Times have been adjusted for range. The effect of the low-velocity anomaly is evident in the centre of the record. First-arrival Pg phases are clear for rays which pass to either side of the caldera region: shots at 0–13 km and 23–40 km on this plot. Between 13 and 26 km, this phase becomes delayed and quickly falls below the noise level. A strong second arrival is visible with a delay of ~0.5 s. This large-amplitude phase is the same one found on record **a** at ranges > 13 km. This record reveals the lateral extent of the low-velocity zone. Thick black lines indicate modelled traveltimes. Time axes are reduced by 7 km s⁻¹ for display purposes.

0.5–1.0 km thick. Thus the crust is probably hotter than our model, and our treatment of the effect of temperature on seismic velocity is conservative (that is, an overestimate).

After removing thermal effects from the velocity-anomaly model, the remaining low velocity is attributed to melt (Fig. 4d). The influence of melt content on velocity depends on the distribution of the melt and assumptions about the principal mechanics. Estimates of velocity as a function of melt fraction have been obtained from numerical^{25–27} and laboratory²⁸ experiments. We use the recent relations of ref. 27, which generally find smaller melt contents than other models. Our minimum estimates of magma content assume that melt occurs in thin cusped films under relaxed conditions (that is, melt ‘squirt’ equalizes pressure between connected inclusions) (Table 1). Maximum melt estimates assume spherical melt inclusions.

Significant concentrations of melt beneath Axial delineate a magma reservoir. The greatest melt concentrations of 5–25%, depending on the model, occur 2.5–3.5 km below the caldera, consistent with the centre of deformation during the 1998 eruption^{3,4}. At this depth the width of the reservoir is 8 × 12 km,

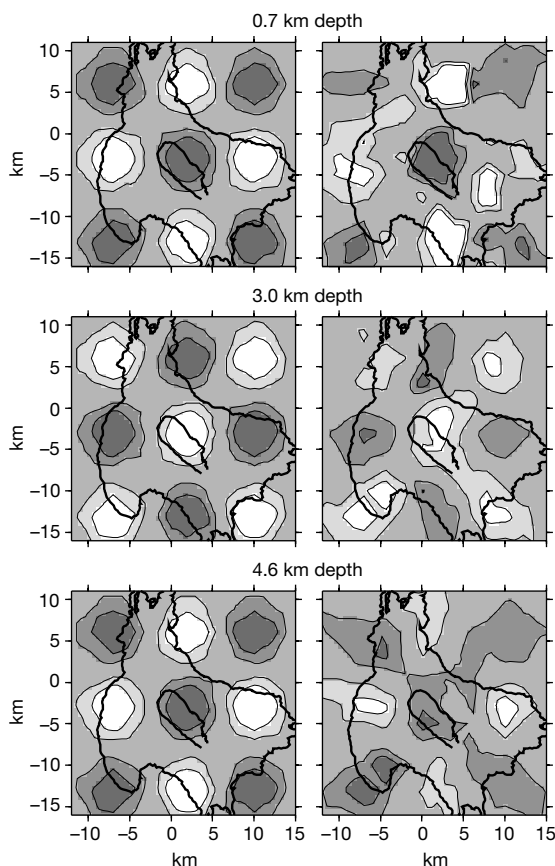


Figure 3 Results of checkerboard resolution tests in a 25 × 25 km box. The synthetic input model (left panels) was created by adding a grid of alternating negative and positive gaussian-shaped anomalies (5%) to the 1D starting model. Travel times were forward-modelled by ray-tracing through this structure using a geometry identical to the one in the real tomographic inversion and assuming similar errors. The same inversion strategy was then applied to the synthetic data set to see how well the input structure could be recovered (right panels). Three depth sections are shown here. The shallow resolution (0.7 km below sea floor) is noisy, though general features are recovered. At depths of the low-velocity zone (3.0 km) the anomalies are well-located. Peak amplitudes are somewhat less than in the input model as a result of smearing. Deeper in the crust (4.6 km) the overall geometry is recovered though smearing is more evident. In the middle and lower crust under the caldera, this test demonstrates our ability to resolve features similar to the observed magma chamber.

elongated similarly to the caldera. We consider these minimum melt contents, as a thin lens of near-pure melt could go undetected owing to intrinsic diffraction effects²⁹. Small amounts of melt, which extend to the bottom of image resolution at 6 km below the sea floor, contribute significantly to the total melt content. The presence of melt in the deep crust suggests either that replenishment of the magma chamber is continuing, or that the crust has yet to

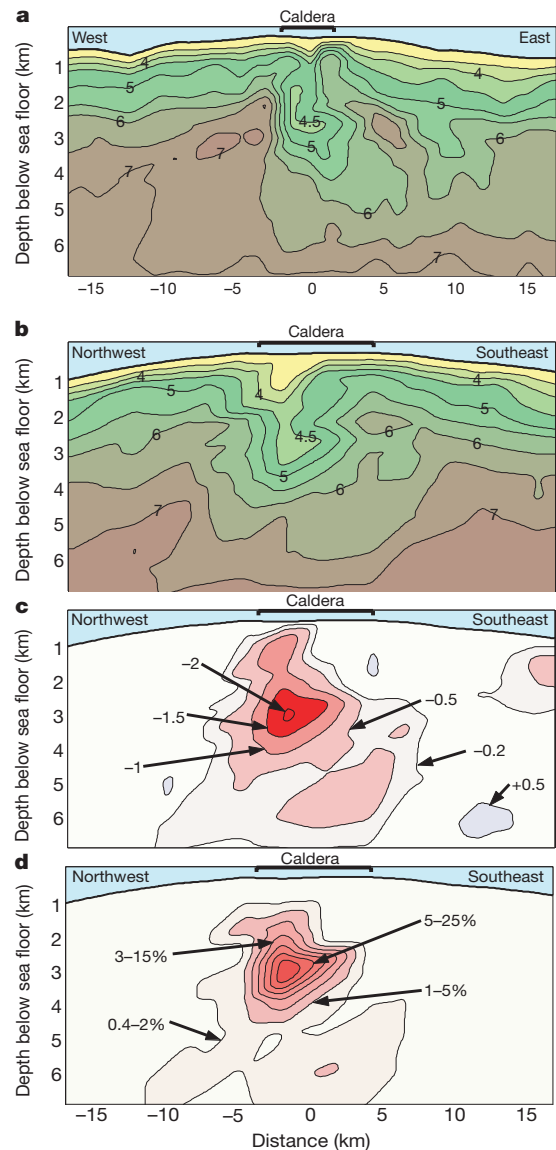


Figure 4 Cross-sectional views of Axial volcano, showing velocity structure and interpretation. **a**, East–west and **b**, northwest–southeast profiles through caldera, as marked in Fig. 1. Compressional-wave velocity is contoured in intervals of 0.5 km s⁻¹. The caldera width is indicated above each panel. Depths are relative to the caldera floor, which is 1.46 km below sea level. The low-velocity zone directly beneath the caldera is the result of a partially molten magma body. These panels show roughly radial symmetry beneath Axial volcano, with features being somewhat elongated along the caldera. The low-velocity zone is not seen to extend away from the caldera in any direction. It does not extend along the rifts or towards the adjacent ridge segments. **c**, Velocity anomaly plot of the northwest–southeast profile. Contours show the difference between the final 3D velocity structure and the 1D bathymetry-draped starting model that characterizes the structure away from the caldera. **d**, After removing the velocity anomaly that could be due to thermal differences, the remaining anomaly is attributed to melt. The different shape of the melt region in **d** and the velocity anomaly in **c** is due to the removal of thermal effects. Comparison with the modelled geothermal gradient removes more of the velocity anomaly at shallower depths.

cool below the solidus following the last replenishment from the mantle.

Even conservative models predict several cubic kilometres of magma beneath Axial volcano. The total melt volume is found by summing the partial melt in the reservoir. The end-member models discussed above yield total magma contents of 5–21 km³ spread throughout a 250-km³ reservoir. Because the bottom of this reservoir is not imaged here, the total volume may be larger still. The amount of magma can best be understood by comparing it to the volume emplaced during eruptions. The magma currently stored beneath Axial volcano is 25–200 times larger than the 0.1–0.2 km³ total estimated volume of the 1998 eruption^{3,4}. There is far more magma than can be removed by several eruptions, implying that stored magma is a long-lived feature at Axial even between eruptive cycles. Individual eruptions do not empty, or even significantly deplete, the reservoir. The small observed melt fractions probably rule out large-scale convective overturn in the magma chamber. However, Axial erupts remarkably homogeneous basalts compared to nearby segments of the Juan de Fuca ridge³⁰, suggesting that some mixing does occur. If mixing occurs in even a portion of the magma reservoir, the smoothing effect on chemical variations could be significant because the melt content is so much larger than the typical eruption size. In light of the lengthy implied residence time, some degree of mixing seems possible.

The residence time in the crust depends on the total magma content and the flux. The observation of large amounts of melt under Axial volcano bolsters previous observations that the volcano provides much of the magma required to accommodate spreading across its rift zones to the north and south. The dimensions of the rift zones can be used to estimate the flux of magma through the Axial system. Assuming that Axial's 100-km rift system is fed primarily from this central magma chamber, and that the rifts are opening at 5–6 cm yr⁻¹ as is the rest of the ridge, an event similar to the one in 1998 is needed on the order of every ten years. If either of these assumptions is incorrect, the flux will decrease accordingly. Combining the flux with the reservoir estimates suggests an average storage time for magma in the crust of a few hundred to a few thousand years, and possibly much longer. The long residence time for melt beneath the discrete volcanic centre at Axial volcano demonstrates that eruptions are a small perturbation to a much larger semi-permanent magma storage system, which is unconnected to nearby segments of the Juan de Fuca ridge. □

Methods

Tomographic inversion

The velocity field is parametrized on an irregular tetrahedral grid, with horizontal node spacing of 2 × 2 km near the caldera and greater spacing in poorly constrained areas of the model. The grid is vertically sheared to conform to the bathymetry. Average vertical node spacing is 0.4 km in the upper crust, increasing to 1.0 km in the lower part of the model. The water layer and bathymetry, as derived from multibeam sonar, are explicitly prescribed in the model. No water path 'corrections' are required. Velocity within each tetrahedron is a linear gradient of the values specified at the four vertices. Travel times and their Fréchet derivatives as a function of node velocities are calculated by summing the analytic ray-path solutions in each tetrahedron. A linearized damped least-squares inversion, parametrized on the same grid, is used to update the velocity field. As the inversion is parametrized in velocity (as opposed to slowness), which increases from < 4 km s⁻¹ at the top of the model to > 7 km s⁻¹ at the bottom, the damped least-squares approach preferentially accommodates model variation at shallow depths. This counters the tendency of shallow and mid-crustal features to be smeared into deeper crust.

The bathymetrically draped 1D model was improved by applying a 1D constraint to the inversion. Travel times for rays that cross the caldera region were excluded, so the velocity structure represents average crust away from the active volcanic edifice. This was the starting model for 3D inversions and the reference model against which anomalies are assessed.

The shadow zones illustrated in Fig. 2 provide much of the 0.181-s r.m.s. error in the 1D travel-time predictions. Three iterations of the inversion using the full set of Pg travel times reduced this misfit to 0.089 s. An empirically derived inversion damping of 0.1|G^TG|_∞, where G is the matrix of Fréchet derivatives, G^T is its matrix transpose, and ||·||_∞ is the L_∞ matrix norm, achieved the greatest misfit reduction while introducing the least model complexity (as measured by the variance of the difference between the final and starting models). Although further reductions could be achieved with decreased inversion

damping and more iterations, the small improvements did not warrant the greater model complexity.

The model resolution was assessed by inverting travel times from synthetic input models using an identical ray geometry and the same inversion strategy as above. Synthetic models contained a grid of 3D gaussian-shaped anomalies of alternating sign. These tests demonstrate our ability to resolve features 5–10 km in diameter to depths of 5–6 km below the sea floor in the vicinity of the caldera (Fig. 3).

Received 30 July; accepted 10 September 2001.

- Johnson, H. P. & Embley, R. W. Axial seamount: An active ridge axis volcano on the central Juan de Fuca ridge. *J. Geophys. Res.* **95**, 12689–12696 (1990).
- Embley, R. W., Chadwick, W. W. Jr, Clague, D. A. & Stakes, D. 1998 eruption of Axial Volcano; multibeam anomalies and seafloor observations. *Geophys. Res. Lett.* **26**, 3425–3428 (1999).
- Chadwick, W. W. Jr, Embley, R. W., Milburn, H. B., Meinig, C. & Stapp, M. Evidence for deformation associated with the 1998 eruption of Axial Volcano, Juan de Fuca ridge, from acoustic extensometer measurements. *Geophys. Res. Lett.* **26**, 3441–3444 (1999).
- Fox, C. G., Chadwick, W. W. Jr & Embley, R. W. Direct observation of a submarine volcanic eruption from a sea-floor instrument caught in a lava flow. *Nature* **412**, 727–729 (2001).
- Desonie, D. L. & Duncan, R. A. The Cobb-Eickelberg seamount chain; hotspot volcanism with mid-ocean ridge basalt affinity. *J. Geophys. Res.* **95**, 12697–12711 (1990).
- Hooff, E. E. & Detrick, R. S. Relationship between axial morphology, crustal thickness, and mantle temperature along the Juan de Fuca and Gorda Ridges. *J. Geophys. Res.* **100**, 22499–22508 (1995).
- Tolstoy, M., Vernon, F. L., Orcutt, J. A. & Wyatt, F. K. The breathing of the seafloor: Tidal correlations of seismicity at Axial Volcano. *Geology* (submitted).
- Dziak, R. P. & Fox, C. G. Long-term seismicity and ground deformation at Axial Volcano, Juan de Fuca Ridge. *Geophys. Res. Lett.* **26**, 3641–3644 (1999).
- Dziak, R. P. & Fox, C. G. The January 1998 earthquake swarm at Axial Volcano, Juan de Fuca Ridge: Hydroacoustic evidence of seafloor volcanic activity. *Geophys. Res. Lett.* **26**, 3429–3432 (1999).
- Fox, C. G. In situ ground deformation measurements from the summit of Axial Volcano during the 1998 volcanic episode. *Geophys. Res. Lett.* **26**, 3437–3440 (1999).
- Hildebrand, J. A. et al. A seafloor and sea surface gravity survey of Axial Volcano. *J. Geophys. Res.* **95**, 12751–12763 (1990).
- Webb, S. C., Deaton, T. K. & Lemire, J. C. A broadband ocean-bottom seismometer system based on a 1-Hz natural period geophone. *Bull. Seismol. Soc. Am.* **91**, 304–312 (2001).
- Cudrak, C. F. & Clowes, R. M. Crustal structure of Endeavour Ridge segment, Juan de Fuca Ridge, from a detailed seismic refraction survey. *J. Geophys. Res.* **98**, 6329–6349 (1993).
- Sohn, R. A., Webb, S. C., Hildebrand, J. A. & Cornuelle, B. D. Three-dimensional tomographic velocity structure of upper crust, CoAxial segment, Juan de Fuca Ridge; implications for on-axis evolution and hydrothermal circulation. *J. Geophys. Res.* **102**, 17679–17695 (1997).
- Dawson, P. B., Chouet, B. A., Okubo, P. G., Villaseñor, A. & Benz, H. M. Three-dimensional velocity structure of the Kilauea caldera. *Geophys. Res. Lett.* **26**, 2805–2808 (1999).
- Dunn, R. A., Toomey, D. R. & Solomon, S. C. Three-dimensional seismic structure and physical properties of the crust and shallow mantle beneath the East Pacific Rise at 9°30'N. *J. Geophys. Res.* **105**, 23537–23555 (2000).
- Canales, J. P., Collins, J. A., Escartin, J. & Detrick, R. S. Seismic structure across the rift valley of the Mid Atlantic Ridge at 23°20' (MARK area): Implications for crustal accretion processes at slow spreading ridges. *J. Geophys. Res.* **105**, 28411–28425 (2000).
- Sinton, J. M. & Detrick, R. S. Mid-ocean ridge magma chambers. *J. Geophys. Res.* **97**, 197–216 (1992).
- Henstock, T. J., Woods, A. W. & White, R. S. The accretion of oceanic crust by episodic sill intrusion. *J. Geophys. Res.* **98**, 4143–4161 (1993).
- Christensen, N. I. Compressional wave velocities in rocks at high temperatures and pressures, critical thermal gradients, and crustal low-velocity zones. *J. Geophys. Res.* **84**, 6849–6857 (1979).
- Karato, S. Importance of anelasticity in the interpretation of seismic tomography. *Geophys. Res. Lett.* **20**, 1623–1626 (1993).
- Kampfmann, W. & Berckhemer, H. High temperature experiments on the elastic and anelastic behaviour of magmatic rocks. *Phys. Earth Planet. Inter.* **40**, 223–247 (1985).
- Chen, W. P. & Molnar, P. Focal depths for intracontinental and intraplate earthquakes and their implications for the thermal and mechanical properties of the lithosphere. *J. Geophys. Res.* **88**, 4183–4214 (1983).
- Huang, P. Y. & Solomon, S. C. Centroid depths of mid-ocean ridge earthquakes: dependence on spreading rate. *J. Geophys. Res.* **93**, 13445–13477 (1988).
- Schmelzig, H. Numerical models on the influence of partial melt on elastic, anelastic and electric properties of rocks. Part I: elasticity and anelasticity. *Phys. Earth Planet. Inter.* **41**, 34–57 (1985).
- Mainprice, D. Modelling the anisotropic seismic properties of partially molten rocks found at mid-ocean ridges. *Tectonophysics* **279**, 161–179 (1997).
- Hammond, W. C. & Humphreys, E. D. Upper mantle seismic wave velocity: Effects of realistic partial melt geometries. *J. Geophys. Res.* **105**, 10975–10986 (2000).
- Sato, H., Sacks, I. S. & Murase, T. The use of laboratory velocity data for estimating temperature and partial melt fraction in the low-velocity zone; comparison with heat flow and electrical conductivity studies. *J. Geophys. Res.* **94**, 5689–5704 (1989).
- Wilcock, W. S. D., Dougherty, M. E., Solomon, S. C., Purdy, G. M. & Toomey, D. R. Seismic propagation across the East Pacific Rise: finite difference experiments and implications for seismic tomography. *J. Geophys. Res.* **98**, 19913–19932 (1993).
- Rhodes, J. M., Morgan, C. & Liias, R. A. Geochemistry of Axial Seamount lavas; magmatic relationship between the Cobb hotspot and the Juan de Fuca Ridge. *J. Geophys. Res.* **95**, 12713–12733 (1990).

Acknowledgements

We thank C. Golden, J. Floyd, D. Bohnenstiehl, V. Ballu, and the crews of the RV *Thomas G. Thompson* and the RV *Maurice Ewing* for efforts at sea; M. Spiegelman, J. Chadwick, M. Perfit and S. Carbotte for discussions; and C. Fox and W. Chadwick for comments on the manuscript. This work was supported by the US National Science Foundation.

Correspondence and requests for materials should be addressed to M.W. (e-mail: mwest@deo.columbia.edu).